PNAS RESEARCH ARTICLE | PHYSICS

Roses in the nonperturbative current response of artificial crystals

Christophe De Beule[a,b,1], Võ Tiến Phong[a], and E. J. Mele[a,1]

Contributed by E. J. Mele; received May 5, 2023; accepted September 12, 2023; reviewed by Leonid Levitov, Hector Ochoa, Mohit Randeria, and Michael P. Zaletel

In two-dimensional artificial crystals with large real-space periodicity, the nonlinear current response to a large applied electric field can feature a strong angular dependence, which encodes information about the band dispersion and Berry curvature of isolated electronic Bloch minibands. Within the relaxation-time approximation, we obtain analytic expressions up to infinite order in the driving field for the current in a band-projected theory with time-reversal and trigonal symmetry. For a fixed field strength, the dependence of the current on the direction of the applied field is given by rose curves whose petal structure is symmetry constrained and is obtained from an expansion in real-space translation vectors. We illustrate our theory with calculations on periodically buckled graphene and twisted double bilayer graphene, wherein the discussed physics can be accessed at experimentally relevant field strengths.

electronic transport | nonlinear response | Hall effect | moiré materials | topological materials

Significance

Moiré and other two-dimensional materials with large-period artificial lattices are ideal platforms for studying electric current responses in the high-field regime. We show that a nonlinearly driven current on a lattice is strongly anisotropic depending on the direction of the driving electric field. We develop an analytical theory of this anisotropy, elucidating its symmetry properties and dependence on the spectral and geometric properties of the underlying electronic Bloch bands.

In two-dimensional (2D) crystals, rotation symmetries about the axis perpendicular to the 2D plane require that the DC current response $\boldsymbol{J}(\boldsymbol{E})$ to a constant uniform electric field $\boldsymbol{E}$ is isotropic to first order in the field strength. Given a crystal symmetry $\mathcal{S}$, the current obeys $\boldsymbol{J}(\mathcal{S}\boldsymbol{E}) = \mathcal{S}\boldsymbol{J}(\boldsymbol{E})$ and unless there are very few symmetries, anisotropies generally occur at higher order (1). Nevertheless, the anisotropy in the current can be a valuable tool for probing the energetic and geometric properties of electron bands. In systems with atomic-scale periodicity, the strong-field regime is not readily accessible because the required fields generally induce interband transitions, i.e., electric breakdown (2), which mask the properties of an otherwise isolated band. However, in moirés (3–5) and superlattice heterostructures (6), such as periodically gated (7) or strained (8) systems, the spatial period of the lattice L can be made large, of the order 10 nm. Hence, a nonperturbative regime, which we define as

$$\omega_B\tau \gg 1, \qquad \omega_B = eEL/\hbar, \tag{1}$$

with ω_B the Bloch frequency and τ the momentum-relaxation time, can be reached for realistic field strengths (9). Taking $L = 10$ nm and $\tau = 1$ ps (10), we find $E \gg 0.66$ kV/cm, which is experimentally feasible. Importantly, the strong-field regime can be realized in these systems well below the onset of electric breakdown, which we estimate as follows. We require $eE\Delta x \ll \varepsilon_{\text{gap}}$ with Δx the uncertainty in the position of the electron, and thus, $eE \ll \varepsilon_{\text{gap}}\hbar\Delta v/|\partial^2\varepsilon/\partial k^2|$. Assuming the curvature is largest near the band edge and that $\Delta v/v$ should be small in the semiclassical theory (2), we find $eEL \ll \varepsilon_{\text{gap}}^2 L/\hbar v < \varepsilon_{\text{gap}}^2/\varepsilon_{\text{width}}$, where $\varepsilon_{\text{width}}$ is the bandwidth. Since moirés and other artificial crystals can host spectrally isolated and narrow minibands, as shown in Fig. 1 *A* and *B* for periodically buckled graphene (PBG) and twisted double bilayer graphene (TDBG), respectively, the right-hand side of this inequality can be made large. For example, taking $L = 10$ nm and $\varepsilon_{\text{gap}}^2/\varepsilon_{\text{width}} = 50$ meV, which we find can be realized in PBG, we obtain $E \ll 50$ kV/cm.

In this work, we investigate the nonperturbative current response in a band-projected theory. That is, we solve the semiclassical transport theory exactly to infinite order in the field strength but assume that interband transitions are negligible, as outlined in the previous paragraph. We focus on trigonal systems with time-reversal ($\mathcal{T}$) symmetry for which $\mathcal{C}_{3z}$ rotation symmetry is conserved but $\mathcal{C}_{2z}$ rotation symmetry and inversion symmetry are broken, i.e., the point groups C_3, C_{3v}, C_{3h}, D_3, and D_{3h} (12). These are the relevant point groups of many moirés and other 2D superlattices, such as those based on graphene (3, 8) and transition-metal dichalcogenides (5). We first consider the weak-field limit and determine the lowest-order anisotropy in the currents from symmetry. There we find a nonlinear Hall response from the Berry curvature hexapole since the lower

Author affiliations: [a]Department of Physics and Astronomy, University of Pennsylvania, Philadelphia, PA 19104; and [b]Department of Physics and Materials Science, University of Luxembourg, Luxembourg L-1511, Luxembourg

Author contributions: C.D.B., V.T.P., and E.J.M. designed research; performed research; analyzed data; and wrote the paper.

Reviewers: L.L., Massachusetts Institute of Technology; H.O., Columbia University; M.R., The Ohio State University; and M.P.Z., University of California.

The authors declare no competing interest.

[1]To whom correspondence may be addressed. Email: cdebeule@sas.upenn.edu or mele@physics.upenn.edu.

This article contains supporting information online at https://www.pnas.org/lookup/suppl/doi:10.1073/pnas.2306384120/-/DCSupplemental.

Published October 19, 2023.

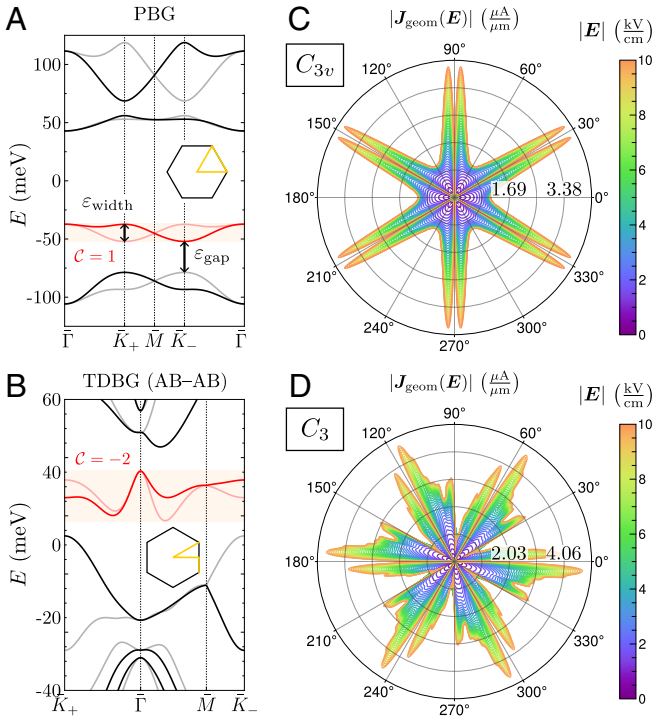

Fig. 1. (*Left*) Energy bands for (*A*) periodically buckled graphene and (*B*) AB–AB twisted double bilayer graphene, along high-symmetry lines in the superlattice Brillouin zone. Dark/light bands correspond to valley K_+/K_-, and the highest valence [lowest conduction] band is shown in red in (*A*) [*B*] with valley Chern number $\mathcal{C}$. (*Right*) Geometric current of the highlighted bands at 0.4 filling and $T = 5$ K for PBG (*C*) and TDBG (*D*). Parameters for PBG are $L/l_0 = 6$, $\mathcal{V}_0 \approx 26$ meV, and $3\phi/\pi = -0.155$ with $\epsilon^2_{\text{gap}}/\epsilon_{\text{width}} = 48$ meV; and for TDBG: $\vartheta = 1.44°$ and $U = 56.5$ meV and others from ref. 11 with $\epsilon^2_{\text{gap}}/\epsilon_{\text{width}} = 4.1$ meV.

order dipole response is forbidden by $\mathcal{C}_{3z}$ and odd powers are forbidden by $\mathcal{T}$. In contrast, the current originating from the band dispersion becomes anisotropic in the transverse response at fifth order while the longitudinal response only depends weakly on the field direction. Furthermore, by expanding in terms of coordination shells, we obtain analytic expressions for the current in terms of the real space Fourier components of the band dispersion and the Berry curvature. This differs from the usual prescription where one expresses the current in terms of multipole moments at successive orders in the response (13, 14). Our results amount to resumming the multipoles to infinite order in the field strength, elucidating the dependence of the current on the field direction. Here, we focus on the current instead of conductivities since the latter are harder to interpret in an arbitrary order in the field strength. For a fixed field strength, we find that the anisotropic current distributions take the form of rose curves when plotted as a function of the field direction, as illustrated in Fig. 1 *C* and *D*. While the longitudinal response has no petals, the main petal structure of the transverse response is determined from symmetry. These petals can fracture into a number of subpetals by breaking in-plane mirrors (or equivalently, out-of-plane π rotations). In a recent work, two of the authors demonstrated that the geometric current originating from the Berry curvature plateaus and dominates in the strong-field limit (15). Here, we obtain the exact plateau values which are strongly anisotropic. We finally apply our theory to graphene-based artificial crystals that host spectrally isolated and narrow minibands: periodically buckled graphene and twisted double bilayer graphene.

Weak-Field Response

It is illustrative to first consider the weak-field limit ($\omega_B\tau \ll 1$) to investigate how symmetry constrains the order at which anisotropy sets in. To this end, we write the current as $\boldsymbol{J} = \boldsymbol{J}^{(+)} + \boldsymbol{J}^{(-)}$, where $\boldsymbol{J}^{(\pm)}(\boldsymbol{E}) \equiv \frac{1}{2}[\boldsymbol{J}(\boldsymbol{E}) \pm \boldsymbol{J}(-\boldsymbol{E})]$ are, respectively, even and odd under field reversal ($\boldsymbol{E} \mapsto -\boldsymbol{E}$). Note that $\boldsymbol{J}^{(+)}$ vanishes if inversion or $\mathcal{C}_{2z}$ symmetry is conserved. In the presence of $\mathcal{C}_{3z}$, the currents can be expanded as

$$J_x^{(-)} + iJ_y^{(-)} = a(E^2)E_+ + bE_-^5 + \mathcal{O}(E^7), \qquad [2]$$

$$J_x^{(+)} + iJ_y^{(+)} = c(E^2)E_-^2 + dE_+^4 + \mathcal{O}(E^6), \qquad [3]$$

where $E_\pm = E_x \pm iE_y$, $a = a_0 + a_1E^2 + a_2E^4$, $c = c_0 + c_1E^2$, and all other parameters are c-numbers. In particular, $a_0 = \sigma_L + i\sigma_H$, where σ_L (σ_H) is the longitudinal (Hall) conductivity. Both sides in Eqs. **2** and **3** transform as angular momentum $L_z = 1$ objects which are conserved mod 3 under $\mathcal{C}_{3z}$ symmetry. If mirror symmetry $\mathcal{M}_x$ ($x \mapsto -x$) is also conserved, one finds that a and b are real while c and d are imaginary, while $\mathcal{M}_y$ ($y \mapsto -y$) makes all parameters real. Time-reversal symmetry further requires that a is real by Onsager reciprocity. Similar expressions were obtained for the odd current in the presence of $\mathcal{C}_{2z}$ or $\mathcal{C}_{4z}$, while $\mathcal{C}_{6z}$ results again in Eq. **2**. These are given in *SI Appendix*, section I C.

The anisotropy in the current is most clearly expressed in terms of the longitudinal $J_\parallel \equiv \hat{E}\cdot\boldsymbol{J}$ and transverse $J_\perp \equiv (\hat{E}\times\hat{z})\cdot\boldsymbol{J}$ current components with $\hat{E} = (\cos\theta, \sin\theta)$ the field direction. This is because $J_\parallel$ ($J_\perp$) transforms as a scalar (pseudoscalar) under a crystal symmetry. For example, for $C_{3v} = \langle \mathcal{C}_{3z}, \mathcal{M}_x\rangle$ (or D_3) and $\mathcal{T}$ symmetry,

$$J_\perp^{(+)} = 2\tilde{c}E^4\cos(3\theta), \qquad [4]$$

$$J_\parallel^{(-)} = aE + bE^5\cos(6\theta), \quad J_\perp^{(-)} = 2bE^5\sin(6\theta), \qquad [5]$$

at leading order with real-valued $\tilde{c} = ic_1$. Here, we have assumed that the even current is purely transverse. Note that the projected currents gain an extra sign under field reversal. The lowest nonzero Hall effect thus originates from the Berry curvature hexapole in a system with $\mathcal{C}_{3z}$ and $\mathcal{T}$ symmetry (14, 16).

Expansion in Coordination Shells

To calculate the current response, we start from the equations of motion for electrons in a 2D crystal (17, 18):

$$\hbar\dot{\boldsymbol{r}}_{\boldsymbol{k}} = \nabla_{\boldsymbol{k}}\varepsilon_{\boldsymbol{k}} - \hbar\dot{\boldsymbol{k}}\times\Omega_{\boldsymbol{k}}\hat{z}, \qquad \hbar\dot{\boldsymbol{k}} = -e\boldsymbol{E}, \qquad [6]$$

where $\Omega_{\boldsymbol{k}} = -2\,\text{Im}\left(\langle\partial u_{\boldsymbol{k}}/\partial k_x|\partial u_{\boldsymbol{k}}/\partial k_y\rangle_{\text{cell}}\right)$ is the Berry curvature with $u_{\boldsymbol{k}}(\boldsymbol{r})$ the cell-periodic Bloch functions in periodic gauge (19), and $\varepsilon_{\boldsymbol{k}}$ is the band dispersion. The steady-state current is given by $\boldsymbol{J} = -2e\int_{\text{BZ}}\frac{d^2\boldsymbol{k}}{(2\pi)^2}f_{\boldsymbol{k}}\dot{\boldsymbol{r}}_{\boldsymbol{k}} \equiv \boldsymbol{J}_{\text{Bloch}} + \boldsymbol{J}_{\text{geom}}$ with $f_{\boldsymbol{k}}$ the nonequilibrium distribution function, obtained from the Boltzmann transport equation. In the relaxation-time approximation, by resumming the solution to all orders in the electric field, we find

$$\boldsymbol{J}_{\text{Bloch}} = \frac{2e}{V_c\hbar}\sum_{\boldsymbol{R}}\frac{i\boldsymbol{R}f^0_{\boldsymbol{R}}\varepsilon_{-\boldsymbol{R}}}{1 - ie\tau\boldsymbol{E}\cdot\boldsymbol{R}/\hbar}, \qquad [7]$$

$$\boldsymbol{J}_{\text{geom}} = (\hat{z}\times\boldsymbol{E})\frac{2e^2}{V_c\hbar}\sum_{\boldsymbol{R}}\frac{f^0_{\boldsymbol{R}}\Omega_{-\boldsymbol{R}}}{1 - ie\tau\boldsymbol{E}\cdot\boldsymbol{R}/\hbar}, \qquad [8]$$

where the sums run over lattice vectors, V_c is the unit cell area, and $\boldsymbol{\varepsilon_R}$, $f^0_{\boldsymbol{R}}$, and $\boldsymbol{\Omega_R}$ are Fourier components with $f^0_{\boldsymbol{k}} = f^0(\boldsymbol{\varepsilon_k})$ the Fermi function. The factor two accounts for spin, as we assume spin–orbit coupling is weak throughout this work.

We now consider a Chern trivial band, separated in energy from other bands, with $C_{3v} = \langle \mathcal{C}_{3z}, \mathcal{M}_x \rangle$ (or D_3) and $\mathcal{T}$ symmetry. Expanding in coordination shells:

$$\boldsymbol{\varepsilon_k} = \sum_{j,n} \varepsilon_j \cos(\boldsymbol{k}\cdot\boldsymbol{L}^{(j)}_n), \quad \boldsymbol{\Omega_k} = \sum_{j,n} \Omega_j \sin(\boldsymbol{k}\cdot\boldsymbol{L}^{(j)}_n), \qquad [9]$$

where j runs over shells and $n = 1, 2, 3$ runs over lattice vectors $\boldsymbol{L}^{(j)}_n$ related by $\mathcal{C}_{3z}$, see Fig. 2*A*. All shells are regular hexagons obtained by scaling and rotating the first shell. Since $\mathcal{T}$ is preserved, $\boldsymbol{\varepsilon_k}$ ($\boldsymbol{\Omega_k}$) is an even (odd) function of momentum. Crystal symmetries $\mathcal{S}$ act as $\boldsymbol{\varepsilon_k} = \boldsymbol{\varepsilon_{\mathcal{S}k}}$ and $\boldsymbol{\Omega_k} = \det(\mathcal{S})\boldsymbol{\Omega_{\mathcal{S}k}}$ and thus constrain the coefficients ε_j and Ω_j.

For example, the second shell contains two lattice vectors related by $\mathcal{C}_{3z}$ and $\mathcal{M}_x$ (or $\mathcal{C}_{2y}$) symmetry, which therefore contribute a term to $\boldsymbol{\Omega_k}$ that is even under $\mathcal{M}_x$. Hence, Ω_2 is forbidden by $\mathcal{M}_x$ but allowed by $\mathcal{M}_y$ (or $\mathcal{C}_{2x}$) which forbids Ω_1. Similarly, only antisymmetric superpositions ($\Omega_4 = -\Omega_5$) of the degenerate fourth and fifth shells are allowed. Conversely, the dispersion conserves $\mathcal{M}_x$ for a symmetric superposition ($\varepsilon_4 = \varepsilon_5$). Plugging the expansions of Eq. **9** into Eqs. **7** and **8**, we obtain

$$J^{\parallel/\perp}_{\text{Bloch}} = -\frac{6eL}{V_c\hbar}\sum_j \frac{\varepsilon_j f^0_j L_j}{L} F^{\parallel/\perp}_{\text{Bloch}}\left(\omega_B\tau L_j/L, \theta+\theta_j\right), \qquad [10]$$

$$J_{\text{geom}} = \frac{6eL}{V_c\tau}\sum_j \frac{\Omega_j f^0_j}{L^2}\frac{L}{L_j} F_{\text{geom}}\left(\omega_B\tau L_j/L, \theta+\theta_j\right), \qquad [11]$$

where $f^0_j = f^0_{\boldsymbol{R}}$ for $\boldsymbol{R} = \boldsymbol{L}^{(j)}_n$. Note that $\mathcal{T}$ implies J_{Bloch} (J_{geom}) is even (odd) in $\boldsymbol{E}$. For the first five shells, the scaling factors $L_j/L = \{1, \sqrt{3}, 2, \sqrt{7}, \sqrt{7}\}$ and angles $\theta_j = \{0, \frac{\pi}{6}, 0, \frac{\pi}{6}+\varphi, \frac{\pi}{6}-\varphi\}$ with $\varphi = \arctan(\frac{\sqrt{3}}{5})$, see Fig. 2*A*. We also defined

$$F^{\parallel}_{\text{Bloch}}(\zeta,\theta) = \frac{\zeta\left[8+6\zeta^2+\zeta^4\cos^2(3\theta)\right]}{16+24\zeta^2+9\zeta^4+\zeta^6\cos^2(3\theta)}, \qquad [12]$$

$$F^{\perp}_{\text{Bloch}}(\zeta,\theta) = \frac{\zeta^5\sin(3\theta)\cos(3\theta)}{16+24\zeta^2+9\zeta^4+\zeta^6\cos^2(3\theta)}, \qquad [13]$$

$$F_{\text{geom}}(\zeta,\theta) = \frac{\zeta^4\left(4+\zeta^2\right)\cos(3\theta)}{16+24\zeta^2+9\zeta^4+\zeta^6\cos^2(3\theta)}, \qquad [14]$$

which are nonperturbative in the field strength. All material details are contained in the coefficients ε_j, f^0_j, and Ω_j. For a fixed field strength E, the currents are roses as a function of the field direction θ. The longitudinal rose, shown in Fig. 2*B*, only has one petal and depends rather weakly on θ. On the other hand, the transverse roses are strongly anisotropic. Both $F^{\perp}_{\text{Bloch}}$ [Fig. 2*C*] and F_{geom} [Fig. 2*D*] have six petals due to $\mathcal{M}_x$ symmetry, while $F^{\perp}_{\text{Bloch}}$ has an extra six petals from $\mathcal{M}_x\mathcal{T}$. As a check, we consider the weak-field limit ($\omega_B\tau \ll 1$) and recover the results from the symmetry analysis. As the field strength increases, $F^{\parallel}_{\text{Bloch}}$ attains a maximum at $(\omega_B\tau)^2 \in [4/3, 2]$ depending on θ, and decays as E^{-1} for $\omega_B\tau \gg 1$. This decrease originates from electrons being Bragg reflected before relaxing to equilibrium and manifests as a negative differential conductance (20). However, unlike the Bloch current, the geometric current plateaus for strong fields (15). This is because the anomalous velocity grows linearly with

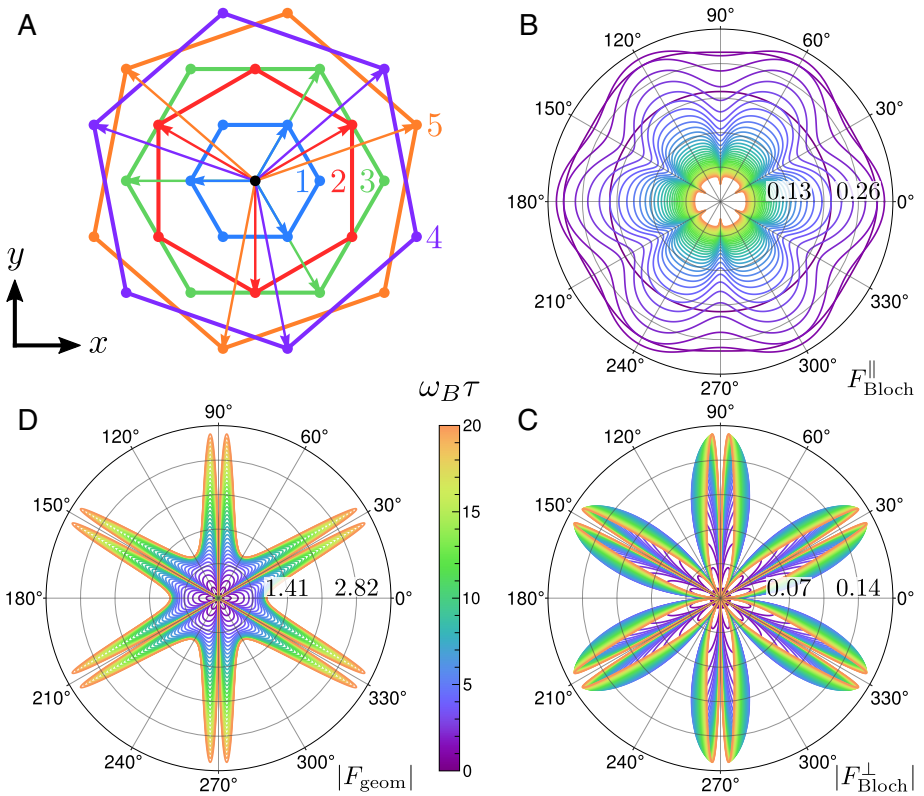

Fig. 2. (*A*) First five coordination shells of the triangular lattice. (*B–D*) First-shell roses for the longitudinal (*B*), transverse Bloch (*C*), and geometric (*D*) current. The color scale gives the value of $\omega_B\tau = e\tau EL/\hbar$.

the field, which cancels the E^{-1} decay. Hence, the geometric current dominates the response at strong field:

$$\lim_{\omega_B\tau\gg 1} J_{\text{geom}} = \frac{6e}{V_c\tau}\sum_j \frac{\Omega_j f_j^0 \delta_{\theta+\theta_j,\pi/6+m\pi/3}}{L_j\cos[3(\theta+\theta_j)]}, \qquad [15]$$

with $m \in \mathbb{Z}$. The plateau value is very singular near $3(\theta + \theta_j) = \pi/2 + m\pi$ where contributions from Ω_j vanish. Terms with different θ_j can thus be distinguished by their dependence on the field direction. Moreover, because the geometric current first increases in magnitude and then plateaus, the geometric differential conductance attains an extremum. For the first shell, it lies at $\omega_B\tau \approx 1.477$ for $\theta = m\pi/3$ and shifts to larger fields when $\theta \to \pi/6 + m\pi/3$.

Experimentally, one can distinguish between the Bloch and geometric currents since they are odd and even in the electric field when $\mathcal{T}$ is conserved, respectively. Moreover, assuming the first shell dominates, which holds in the case of periodically buckled graphene (*Material Systems*), the ratios

$$\frac{J^{\perp}_{\text{Bloch}}}{J^{\parallel}_{\text{Bloch}}} \simeq \frac{(\omega_B\tau)^4\sin(3\theta)\cos(3\theta)}{8+6(\omega_B\tau)^2+(\omega_B\tau)^4\cos^2(3\theta)}, \qquad [16]$$

$$\frac{J^{\perp}_{\text{Bloch}}}{J_{\text{geom}}} \simeq -\frac{\varepsilon_1\tau L^2}{\hbar\Omega_1}\frac{\omega_B\tau\sin(3\theta)}{4+(\omega_B\tau)^2}, \qquad [17]$$

are independent of the chemical potential and yield τ and ε_1/Ω_1. Measuring J_{geom} at different fillings of the band would then, in principle, yield Ω_1 and ε_1. The inverse problem of extracting the Fourier coefficients from the response is generally more tractable when $\boldsymbol{\Omega}_{\boldsymbol{k}}$ and $\boldsymbol{\varepsilon}_{\boldsymbol{k}}$ are sufficiently smooth such that only a limited number of shells contribute.

Material Systems

We apply the nonperturbative response theory to PBG (C_{3v}) and TDBG (D_3 and C_3). In both systems, the band structure is tunable by applying an electric field normal to the xy plane. We calculate $\varepsilon^2_{\text{gap}}/\varepsilon_{\text{width}}$ for the highest valence band and the lowest conduction band of a given valley and find broad windows in the strong-field regime where the band-projected theory is valid, i.e.,

$$\frac{0.66\,\text{ps}}{\tau}\frac{10\,\text{nm}}{L} \ll \frac{E}{\text{kV/cm}} \ll \frac{\varepsilon^2_{\text{gap}}}{\varepsilon_{\text{width}}\,\text{meV}}\frac{10\,\text{nm}}{L}. \qquad [18]$$

Other potential material realizations include periodically gated Bernal bilayer graphene (21) and moirés based on transition-metal dichalcogenides (5). Moreover, large nonlinear responses have already been studied both theoretically and experimentally in twisted bilayer graphene, where a second-order Hall effect is possible when both $\mathcal{C}_{2z}$ and $\mathcal{C}_{3z}$ are broken either due to disorder (22) or strain (23–25).

We further consider the case where the buckling pattern (PBG) or the moiré lattice (TDBG) varies slowly with respect to the atomic lattice. Hence, the two valleys of graphene ($K_{\pm}$) are effectively decoupled. The total current is then obtained by summing contributions from both valleys, resulting in a small modification of the expressions in Eqs. **7** and **8**. Since the valleys are related by $\mathcal{T}$, the total current is obtained by letting $f^0_{\boldsymbol{R}}\varepsilon_{-\boldsymbol{R}} \mapsto 2\,\text{Re}\left(f^{0+}_{\boldsymbol{R}}\varepsilon^{+}_{-\boldsymbol{R}}\right)$ in the Bloch current and $f^0_{\boldsymbol{R}}\Omega_{-\boldsymbol{R}} \mapsto 2\,\text{Im}\left(f^{0+}_{\boldsymbol{R}}\Omega^{+}_{-\boldsymbol{R}}\right)$ in the geometric current where the superscript corresponds to valley K_+. This modification does not change Eq. **16** but gives an extra factor from the phases of the Fourier components in Eq. **17**. A shell expansion for two decoupled bands, which individually break $\mathcal{T}$ and carry valley Chern numbers, is given in *SI Appendix*, section II E.

Periodically Buckled Graphene. When monolayer graphene is placed on top of $NbSe_2$ or hBN (8, 26) as well as artificial nanobubble (27) or nanopillar (28–30) substrates, it can undergo a buckling transition. Here, we consider a substrate-induced buckling transition that gives rise to a periodic height profile with C_{3v} symmetry. In the first-star approximation, the height profile is given by $h(\boldsymbol{r}) = h_0\sum_{n=1}^{3}\cos\left(\mathcal{G}_n\cdot\boldsymbol{r}+\frac{\pi}{4}+\phi\right)$ with $\mathcal{G}_n = \mathcal{C}_{3z}^{n-1}(0, 4\pi/\sqrt{3}L)$, where the phase ϕ controls the shape of the profile (8, 30–32). Experimentally, ϕ can be tuned by designing different artificial substrates. When $h(\boldsymbol{r})$ varies slowly on the graphene lattice scale ($L \gg a = 0.246$ nm), a valley-projected theory can be used with Hamiltonian (30)

$$\mathcal{H}_\nu = \hbar v_F\left[\boldsymbol{k}+\frac{\nu e}{\hbar}\mathcal{A}(\boldsymbol{r})\right]\cdot\left(\nu\sigma_x,\sigma_y\right)+\mathcal{V}(\boldsymbol{r})\sigma_0, \qquad [19]$$

where $\nu = \pm 1$ indicates the valleys K_ν and $v_F = \sqrt{3}\,t_0 a/2$ is the Fermi velocity with $t_0 = 2.7$ eV (33). Here, the scalar field $\mathcal{V} = \mathcal{V}_0\sum_{n=1}^{3}\cos\left(\mathcal{G}_n\cdot\boldsymbol{r}+\frac{\pi}{4}+\phi\right)$ originates from applying an electric field (different from the driving field) normal to the nominal graphene plane (34) and $\mathcal{B} = \nabla\times\mathcal{A} = \hat{z}\mathcal{B}(\boldsymbol{r})$ with $\mathcal{B}(\boldsymbol{r}) = \mathcal{B}_0\sum_{n=1}^{3}\cos\left(\mathcal{G}_n\cdot\boldsymbol{r}-2\phi\right)$ the strain-induced pseudomagnetic field (PMF). The latter is obtained by taking into account in-plane relaxation while keeping the height modulation fixed (30) (*SI Appendix*, section III A). Up to a translation, the PMF is invariant under $\phi \mapsto \phi + \pi/3$ while $\mathcal{V}$ changes sign. Hence, we restrict ourselves to $\phi \in (-\pi/6, \pi/6]$. For concreteness, we take $L/l_0 = 6$ with $L = 14$ nm, where $l_0 = \sqrt{\hbar/e\mathcal{B}_0} \propto \sqrt{aL^3/h_0^2}$ is an effective magnetic length. These are the experimental values of ref. 8. Furthermore, because $\sigma_z\mathcal{H}_\nu[\mathcal{V}]\sigma_z = -\mathcal{H}_\nu[-\mathcal{V}]$, we only consider the highest valence band (of both valleys) for PBG.

In Fig. 3*A*, we show $\varepsilon^2_{\text{gap}}/\varepsilon_{\text{width}}$ in the $(\mathcal{V}_0, \phi)$ plane for the highest valence band. By varying the shape of the height profile and the electric field normal to the nominal graphene plane, this ratio is in the range 10 to 100 meV which should be large enough to avoid electric breakdown in the strong-field regime. As an example, we consider the parameters indicated with a cross on Fig. 3*A*. For this case, the valley Chern number is given by ± 1 for valley $K_\pm$, and the bands along high-symmetry lines are shown in Fig. 1*A*. In Fig. 3*B*, we show the relative magnitude and phase of the Fourier components $\varepsilon^+_{\boldsymbol{R}}$ and $\Omega^+_{\boldsymbol{R}}$. We see that the first shell dominates in this particular case. The longitudinal and geometric current as well as the corresponding differential conductance are shown in Fig. 3*C* for different fillings of the band. We find that the strong-field regime is reached for $E \approx 1$ kV/cm. The longitudinal current does not depend strongly on the field direction; hence, we only show the case $\theta = 0°$. Here, the E^{-1} decay for $\omega_B\tau \gg 1$ manifests as a negative differential conductance. On the other hand, the geometric current is strongly anisotropic, as is clear from the current rose shown in Fig. 1*C*. We see that the plateau in the geometric current shifts to larger fields as we increase θ from 0° to 20°, concomitant with a shift and broadening of the peak in the differential conductance.

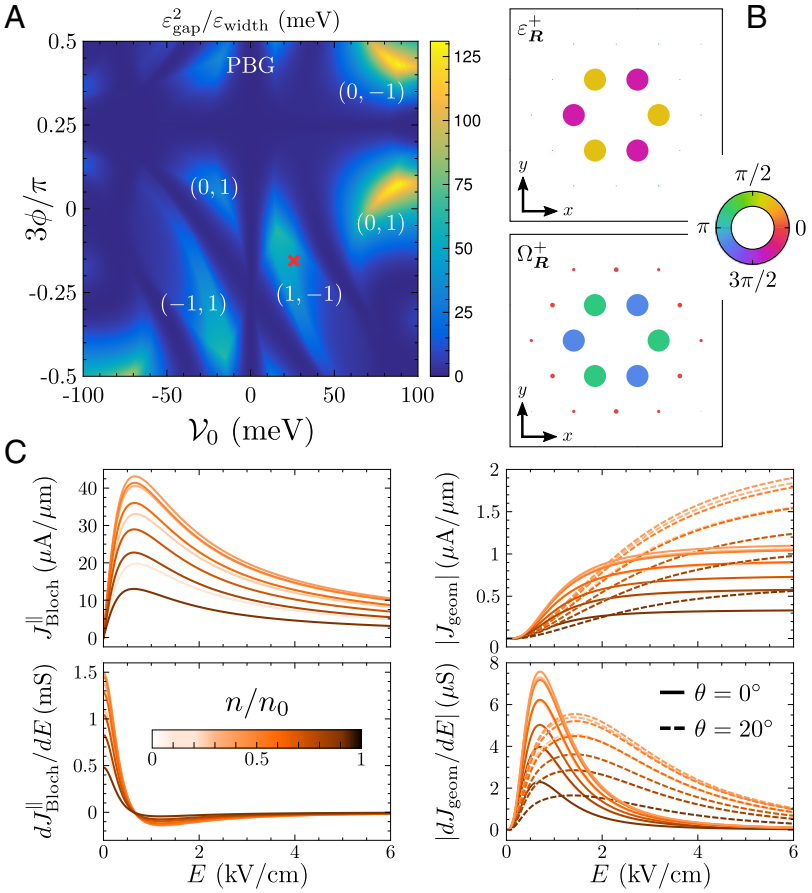

Fig. 3. (*A*) $\epsilon^2_{\rm gap}/\epsilon_{\rm width}$ for the highest valence band of PBG in the $(\mathcal{V}_0, \phi)$ plane. The cross corresponds to the case shown in Fig. 1*A*. Some K_+ valley Chern numbers of the two bands near charge neutrality are shown. (*B*) Relative magnitude and phase of $\epsilon^+_{\boldsymbol{R}}$ and $\Omega^+_{\boldsymbol{R}}$ for the cross in (*A*). (*C*) $J^{\parallel}_{\rm Bloch}$ for field direction $\theta = 0°$ and $|J_{\rm geom}|$ for $\theta = 0°$ (solid) and $\theta = 20°$ (dashed), as well as the differential conductance, for $T = 5$ K. The color scale gives the filling n/n_0 of the band.

Twisted Double Bilayer Graphene. TDBG consists of a stack of two (AB or BA) Bernal bilayer graphene layers that are twisted relative to each other (11, 35). A second-order Hall effect was recently observed in TDBG for twist angles $\theta \sim 1°$ where $\mathcal{C}_{3z}$ was broken by strain (36–39), making this system a promising platform for studying nonperturbative responses. For such small twists, one can again use a valley-projected theory; see *SI Appendix*, section IV. The tunable parameters for TDBG are now given by the twist angle ϑ and the bias difference U between the *topmost* and *bottommost* layer due to an applied electric field (different from the driving field) normal to the TDBG plane. The latter reduces the point group of TDBG from D_3 to C_3. As such, the current roses are less constrained and only show $\mathcal{C}_{3z}$ symmetry; see Fig. 1*D*.

In Fig. 4*A*, we show $\epsilon^2_{\rm gap}/\epsilon_{\rm width}$ in the (U, ϑ) plane for the lowest conduction band. By varying the twist angle and the bias, this ratio can be of the order of 5 meV which limits the range of electric fields where the band-projected theory is valid in the strong-field regime to a few kV/cm. We note that this ratio can be larger for smaller twist angles $\vartheta \ll 1°$. However, for such small twists, lattice relaxation might become important, and as such, we do not consider them here. As an example, we consider the parameters indicated with a cross on Fig. 4*A*. For this case, the valley Chern number is given by ∓ 2 for valley $K_\pm$, and the bands along high-symmetry lines are shown in Fig. 1*B*. In Fig. 4*B*, we show the relative magnitude and phase of the Fourier components $\epsilon^+_{\boldsymbol{R}}$ and $\Omega^+_{\boldsymbol{R}}$ up to the fifth shell. Contrary to the case chosen for PBG in Fig. 3, many shells contribute. The longitudinal and geometric current as well as the corresponding differential conductance are shown in Fig. 4*C* for different fillings of the band. Because the moiré lattice constant $L_m(\vartheta = 1.44°) \approx 9.8$ nm is of the same order as the one chosen for PGB and the first shell is still the largest contribution, the onset of the strong-field regime is again given by $E \approx 1$ kV/cm. Generically, the longitudinal current does not depend strongly on the field direction; hence, we only show the case $\theta = 0°$. On the other hand, as already demonstrated in Fig. 1*D*, the geometric current is strongly anisotropic. The field strength for which $J_{\rm geom}$ plateaus as well as the position and width of the peak in $dJ_{\rm geom}/dE$ is strongly dependent on the field direction. Moreover, since the point group of interlayer-biased TDBG is C_3, there are no mirror axes for which the transverse currents vanish. Hence, there is no fixed field direction for which the plateau is reached first as a function of the field strength.

Discussion

In this work, we have studied the anisotropy in the current response to a static electric field within a semiclassical band-projected theory up to infinite order in the field strength. We have focused on two-dimensional superlattice systems with trigonal symmetry that feature spectrally isolated and narrow minibands, for which electric breakdown is absent even in the strong-field regime. We have demonstrated that the Bloch

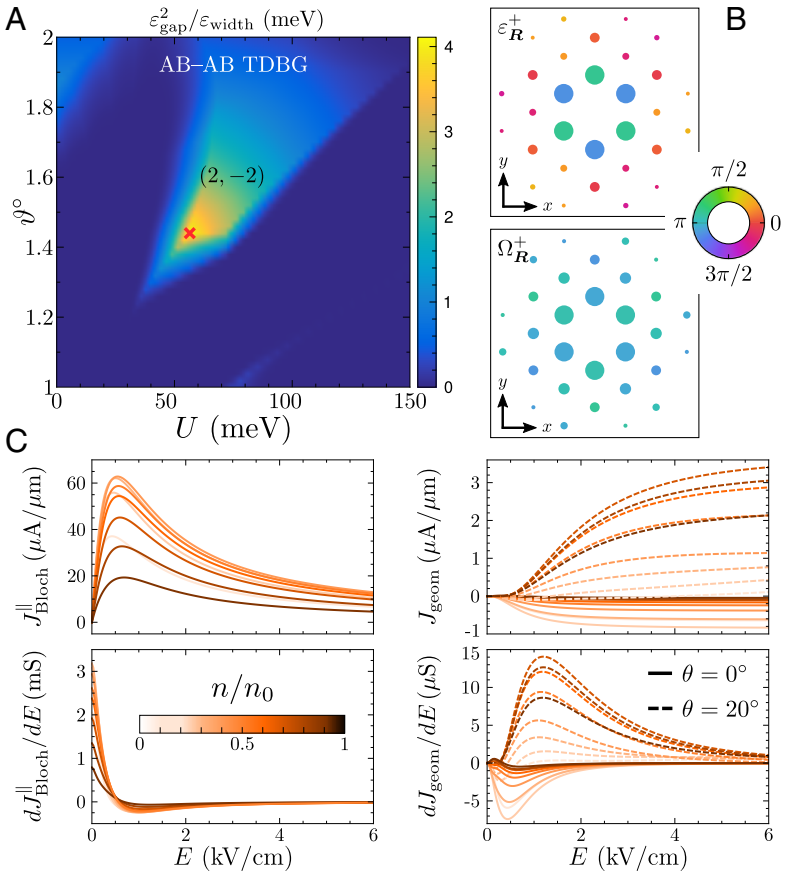

Fig. 4. (*A*) $\epsilon^2_{\rm gap}/\epsilon_{\rm width}$ for the lowest conduction band of AB–AB TDBG in the (U, ϑ) plane. The cross gives the case shown in Fig. 1*B*, and the K_+ valley Chern numbers of the two bands near charge neutrality are shown. (*B*) Relative magnitude and phase of $\varepsilon^+_{\boldsymbol{R}}$ and $\Omega^+_{\boldsymbol{R}}$ for the cross in (*A*) up to the fifth shell. (*C*) $J^{\parallel}_{\rm Bloch}$ for field direction $\theta = 0°$ and $J_{\rm geom}$ for $\theta = 0°$ (solid) and $\theta = 20°$ (dashed), as well as dJ/dE, for $T = 5$ K. The color scale gives the filling n/n_0 of the band.

(geometric) currents can be written in terms of an expansion in coordination shells where each term is given by a rose weighted by the Fourier component of the group velocity (Berry curvature). Here, each rose obeys the symmetries of the given shell. While the longitudinal current rose has no petals and hence a weak anisotropy, the transverse currents are strongly anisotropic. The latter follows from the fact that roses originating from shells with mirror symmetries necessarily have nodes and thus several petals. Furthermore, for the longitudinal and Bloch transverse response, the strong-field regime is characterized by a negative differential conductance due to electrons being Bragg reflected before relaxing their momentum. For the geometric response, however, the current plateaus in the strong-field regime, yielding a peak in the differential conductance whose position and width strongly depend on the field direction.

We have suggested two candidate systems: periodically buckled graphene and twisted double bilayer graphene. For these systems, strong-field responses are accessible at field strengths $E \sim 1$ kV/cm owing to a lattice constant of the order of 10 nm. Importantly, because these systems break $\mathcal{C}_{2z}$ symmetry but conserve time-reversal symmetry, there is a nonlinear geometric response from the momentum distribution of Berry curvature. We have further shown that $\epsilon^2_{\rm gap}/\epsilon_{\rm width} \sim 50$ meV for PBG and $\epsilon^2_{\rm gap}/\epsilon_{\rm width} \sim 5$ meV for AB–AB TDBG, such that especially for the case of PBG, the strong-field regime can be reached well before electric breakdown. Finally, we note that most moiré systems display some degree of heterostrain which breaks rotation symmetry (40). In some cases, this feature is necessary to observe a second-order Hall effect (36–39). Hence, in the presence of strain, the symmetry of the rose pattern at low fields is expected to be reduced, while at larger fields, the petal structure enforced by $\mathcal{C}_{3z}$ symmetry is expected to be only slightly perturbed.

Data, Materials, and Software Availability. All study data are included in the article and/or *SI Appendix*.

ACKNOWLEDGMENTS. We thank S. Gassner for discussions. This research was funded in whole, or in part, by the Luxembourg National Research Fund (FNR project No. 16515716). Work by C.D.B., V.T.P., and E.J.M. is supported by the Department of Energy under grant DE-FG02-84ER45118. V.T.P. acknowledges further support from the P.D. Soros Fellowship for New Americans and the NSF's Graduate Research Fellowships Program.

1. L. Wu *et al.*, Giant anisotropic nonlinear optical response in transition metal monopnictide Weyl semimetals. *Nat. Phys.* **13**, 350–355 (2017).
2. N. W. Ashcroft, N. D. Mermin, *Solid State Physics* (Saunders College Publishing, 1976).
3. E. Y. Andrei, A. H. MacDonald, Graphene bilayers with a twist. *Nat. Mater.* **19**, 1265–1275 (2020).
4. E. Y. Andrei *et al.*, The marvels of moiré materials. *Nat. Rev. Mater.* **6**, 201–206 (2021).
5. K. F. Mak, J. Shan, Semiconductor moiré materials. *Nat. Nanotechnol.* **17**, 686–695 (2022).
6. R. Tsu, *Superlattice to Nanoelectronics* (Elsevier Science, 2005).
7. C. Forsythe *et al.*, Band structure engineering of 2D materials using patterned dielectric superlattices. *Nat. Nanotechnol.* **13**, 566–571 (2018).
8. J. Mao *et al.*, Evidence of flat bands and correlated states in buckled graphene superlattices. *Nature* **584**, 215–220 (2020).
9. A. Fahimniya, Z. Dong, E. I. Kiselev, L. Levitov, Synchronizing bloch-oscillating free carriers in moiré flat bands. *Phys. Rev. Lett.* **126**, 256803 (2021).
10. J. M. Dawlaty, S. Shivaraman, M. Chandrashekhar, F. Rana, M. G. Spencer, Measurement of ultrafast carrier dynamics in epitaxial graphene. *Appl. Phys. Lett.* **92**, 042116 (2008).

11. M. Koshino, Band structure and topological properties of twisted double bilayer graphene. *Phys. Rev. B* **99**, 235406 (2019).
12. M. S. Dresselhaus, G. Dresselhaus, A. Jorio, *Group Theory: Application to the Physics of Condensed Matter* (Springer, 2008).
13. I. Sodemann, L. Fu, Quantum nonlinear hall effect induced by Berry curvature dipole in time-reversal invariant materials. *Phys. Rev. Lett.* **115**, 216806 (2015).
14. C. P. Zhang, X. J. Gao, Y. M. Xie, H. C. Po, K. T. Law, Higher-order nonlinear anomalous Hall effects induced by Berry curvature multipoles. *Phys. Rev. B* **107**, 115142 (2023).
15. Vo. T. Phong, E. J. Mele, Quantum geometric oscillations in two-dimensional flat-band solids. *Phys. Rev. Lett.* **130**, 266601 (2023).
16. N. V. Leppenen, L. E. Golub, Linear photogalvanic effect in surface states of topological insulators. *Phys. Rev. B* **107**, L161403 (2023).
17. M. C. Chang, Q. Niu, Berry phase, hyperorbits, and the Hofstadter spectrum. *Phys. Rev. Lett.* **75**, 1348–1351 (1995).
18. G. Sundaram, Q. Niu, Wave-packet dynamics in slowly perturbed crystals: Gradient corrections and Berry-phase effects. *Phys. Rev. B* **59**, 14915–14925 (1999).
19. D. Vanderbilt, *Berry Phases in Electronic Structure Theory* (Cambridge University Press, 2018).
20. L. Esaki, R. Tsu, Superlattice and negative differential conductivity in semiconductors. *IBM J. Res. Dev.* **14**, 61–65 (1970).
21. S. A. A. Ghorashi *et al*., Topological and stacked flat bands in bilayer graphene with a superlattice potential. *Phys. Rev. Lett.* **130**, 196201 (2023).
22. J. Duan *et al*., Giant second-order nonlinear hall effect in twisted bilayer graphene. *Phys. Rev. Lett.* **129**, 186801 (2022).
23. P. A. Pantaleón, T. Low, F. Guinea, Tunable large Berry dipole in strained twisted bilayer graphene. *Phys. Rev. B* **103**, 205403 (2021).
24. P. A. Pantaleón, Vo. T. Phong, G. G. Naumis, F. Guinea, Interaction-enhanced topological Hall effects in strained twisted bilayer graphene. *Phys. Rev. B* **106**, L161101 (2022).
25. C. P. Zhang *et al*., Giant nonlinear Hall effect in strained twisted bilayer graphene. *Phys. Rev. B* **106**, L041111 (2022).
26. S. P. Milovanović, M. Andelković, L. Covaci, F. M. Peeters, Band flattening in buckled monolayer graphene. *Phys. Rev. B* **102**, 245427 (2020).
27. Z. Qi *et al*., Pseudomagnetic fields in graphene nanobubbles of constrained geometry: A molecular dynamics study. *Phys. Rev. B* **90**, 125419 (2014).
28. Y. Jiang *et al*., Visualizing strain-induced pseudomagnetic fields in graphene through an hBN magnifying glass. *Nano Lett.* **17**, 2839–2843 (2017).
29. D. H. Kang *et al*., Pseudo-magnetic field-induced slow carrier dynamics in periodically strained graphene. *Nat. Commun.* **12**, 5087 (2021).
30. V. T. Phong, E. J. Mele, Boundary modes from periodic magnetic and pseudomagnetic fields in graphene. *Phys. Rev. Lett.* **128**, 176406 (2022).
31. C. De Beule, V. T. Phong, E. J. Mele, Network model for periodically strained graphene. *Phys. Rev. B* **107**, 045405 (2023).
32. M. T. Mahmud, D. Zhai, N. Sandler, Topological flat bands in strained graphene: Substrate engineering and optical control. *Nano Lett.* **23**, 7725–7732 (2023).
33. A. H. Castro Neto, F. Guinea, N. M. R. Peres, K. S. Novoselov, A. K. Geim, The electronic properties of graphene. *Rev. Mod. Phys.* **81**, 109–162 (2009).
34. Q. Gao, J. Dong, P. Ledwith, D. Parker, E. Khalaf, Untwisting moiré physics: Almost ideal bands and fractional Chern insulators in periodically strained monolayer graphene. *Phys. Rev. Lett.* **131**, 096401 (2023).
35. N. R. Chebrolu, B. L. Chittari, J. Jung, Flat bands in twisted double bilayer graphene. *Phys. Rev. B* **99**, 235417 (2019).
36. S. Sinha *et al*., Berry curvature dipole senses topological transition in a moiré superlattice. *Nat. Phys.* **18**, 765–770 (2022).
37. A. Chakraborty *et al*., Nonlinear anomalous Hall effects probe topological phase-transitions in twisted double bilayer graphene. *2D Mater.* **9**, 045020 (2022).
38. J. Zhong *et al*., Effective manipulation and realization of a colossal nonlinear Hall effect in an electric-field tunable moiré system (2023).
39. P. Tiwari *et al*., Observation of the time-reversal symmetric hall effect in graphene-WSe_2 heterostructures at room temperature. *Nano Lett.* **23**, 6792–6798 (2023).
40. Y. Xie *et al*., Spectroscopic signatures of many-body correlations in magic-angle twisted bilayer graphene. *Nature* **572**, 101–105 (2019).